

**MODIFICATIONS OF XRD AT  
HOUGHTON COLLEGE**

By

Heather C. Phillips

A thesis submitted in partial fulfillment of the  
requirements for the degree of

Bachelor of Science

Houghton College

November 2018

Signature of Author.....

Department of Physics  
November 7, 2018

.....  
Dr. Brandon Hoffman  
Associate Professor of Physics  
Research Supervisor

.....  
Dr. Mark Yuly  
Professor of Physics

# CONSTRUCTION OF XRD AT HOUGHTON COLLEGE

By

Heather C. Phillips

Submitted to the Department of Physics  
on November 7, 2018 in partial fulfillment of the  
requirement for the degree of  
Bachelor of Science

## **Abstract**

Modifications and safety features of a 40 kV Bragg–Brentano  $\theta - 2\theta$  x-ray diffractometer (XRD) are being completed at Houghton College for the purpose of studying texture transformations in thin metal films. The sample and detector position are controlled by separate stepper motors that drive along a semicircular track. A radiation monitor measures the number of x-ray counts while scanning along the track. Using Bragg's law, the out-of-plane lattice distance of various crystal orientations is correlated to certain values of  $2\theta$ . Comparing the area fraction of the integrated peak intensities, the texture of the thin metal film can be determined.

Thesis Supervisor: Dr. Brandon Hoffman  
Title: Associate Professor of Physics

## TABLE OF CONTENTS

<b>Chapter 1 Introduction .....</b>	<b>5</b>
<b>1.1. History.....</b>	<b>5</b>
1.1.1. Discovery of X-rays.....	5
1.1.2. Laue's Discovery .....	6
1.1.3. X-Ray Diffraction (XRD) Development .....	8
<b>1.2. XRD Thin Metal Film Research at Houghton College .....</b>	<b>10</b>
1.2.1. Thin Metal Films.....	10
1.2.2. Driving Force of Texture Transformation Research .....	14
1.2.3. XRD at Houghton College .....	16
<b>Chapter 2 Theory .....</b>	<b>18</b>
<b>2.1. X-ray Production .....</b>	<b>18</b>
2.1.1. Bremsstrahlung x-ray.....	18
2.1.2. Characteristic X-ray.....	19
<b>2.2. Wave interference.....</b>	<b>19</b>
<b>2.3. Bragg's Law.....</b>	<b>23</b>
<b>2.4. Correction Factor .....</b>	<b>25</b>
2.4.1. Structure Factor.....	26
2.4.2. Atomic Form Factor .....	28
2.4.3. Lorentz Factor .....	28
2.4.4. Attenuation Factor.....	30
2.4.5. Polarization Factor .....	31
2.4.6. Overall Correction.....	31
<b>Chapter 3 Design.....</b>	<b>33</b>
<b>3.1. Overview .....</b>	<b>33</b>
<b>3.2. Basic Design .....</b>	<b>33</b>
3.2.1. Table.....	33
3.2.2. X-ray Production .....	34
<b>3.3. LabVIEW Programs.....</b>	<b>35</b>
3.3.1. Long Scan .....	36
3.3.2. Constant $\theta$ .....	36
<b>3.4. Safety Features.....</b>	<b>36</b>
3.4.1. Plexiglass Box .....	36
3.4.2. Steel Shielding.....	36
<b>Chapter 4 Results and Discussion.....</b>	<b>38</b>
<b>4.1. Testing the XRD.....</b>	<b>38</b>
4.1.1. Set up .....	38
4.1.2. Results .....	38
<b>4.2. Future Plans.....</b>	<b>40</b>
4.2.1. Extra Safety Features.....	40
4.2.2. Improve the motor reproducibility.....	40
4.2.3. Improve the radiation count.....	40

## TABLE OF FIGURES

Figure 1: Diagram of the evacuated tube used by Plücker. ....	5
Figure 2: Picture of Röntgen's wife's hand.....	6
Figure 3: Laue, Friedrich, and Knipping's first successful image. ....	7
Figure 4: Picture of Laue, Friedrich, and Knipping's x-ray diffraction apparatus. ....	8
Figure 5: Bragg's first setup of the X-ray Spectrometer. ....	9
Figure 6: Diagram of the structure of a face-centered cubic.....	10
Figure 7: The normal planes of (100) on the left and (111) on the right.....	11
Figure 8: Top view of the arrangement of atoms for (100) and (111). ....	11
Figure 9: Diagram showing how an EBPVD creates a sample.....	12
Figure 10: Images showing two general types of texture transformation. ....	13
Figure 11: Diagram showing the formation of twin boundary. ....	14
Figure 12: Graph of the fraction of the film that is in the (111) orientation. ....	15
Figure 13: Diagram showing the difference of the (100) and (111) nanotwins. ....	16
Figure 14: Fractional integrated intensity of (111) versus thickness for Ag films. ....	16
Figure 15: Diagram showing how a Bremsstrahlung x-ray is produced.....	19
Figure 16: Graph of the photon counts for a spectrum of energies of x-rays produced. ....	21
Figure 17: Diagram of the first step of producing a characteristic x-ray. ....	21
Figure 18: Diagram of the second step of producing a characteristic x-ray. ....	22
Figure 19: Example graph of constructive interference.....	22
Figure 20: Example graph of deconstructive interference.....	23
Figure 21: An example of a general wave interference.....	23
Figure 22: Diagram demonstrating the usage of Bragg's Law.....	25
Figure 23: The right triangle found in Figure 22.....	25
Figure 24: Vector diagram that satisfy Equation 12. ....	29
Figure 25: Diagram showing the triangle of Figure 24 and the velocity vector.....	30
Figure 26: Diagram of the basic design of the.....	34
Figure 27: Figure of the actual table.....	34
Figure 28: Diagram of the circuit.....	35
Figure 29: Figure of the copper target and filament.....	35
Figure 30: Radiation count vs 2-theta graph for constant theta of 36°. ....	39
Figure 31: Radiation count vs 2-theta graph for constant theta of 35°. ....	39

## Chapter 1

### INTRODUCTION

#### 1.1. History

##### 1.1.1. Discovery of X-rays

In 1859, Julius Plücker used an evacuated Crookes tube set up, as shown in Figure 1, to study the electrical discharge produced that travels from the cathode to the anode. During the experiment, he made an observation of a bright luminescence that occurred on the cathode side of the tube. This effect was unexpected because nothing was expected to leave the glass tube. He also noticed that the luminescence location and shape was changed when he put a magnet close by the tube. He explained this observation in a paper [1] and sparked an interest among physicists.

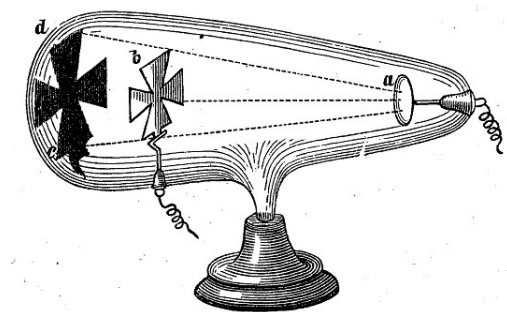


Figure 1: Diagram of the evacuated tube used by Plücker. When a charged coil is connected to the wires shown, an electrical discharge is created. The discharge travels from the cathode (a) to target (b). A shadow is formed as shown at (c) and (d). Figure taken from Ref [2].

After some time and experiments, physicists started to realize that there was something invisible causing the calcite or fluorite to glow. This invisible thing later became described as rays. Forty years later, a physicist named Wilhelm Röntgen decided to investigate the cathode rays. At this point, other physicists had determined that the intensity of the fluorescence, the bright light, depends on the voltage used and the material of the cathode and target [3]. It was also commonly known that the rays are absorbed in gases and metal

foils. Looking into this topic, Röntgen [4] got a discharge tube and sealed it inside of a cardboard box. Once the set up was completed and the tube was turned on, he noticed that a barium platino cyanide sheet laying on a table a distance away from the tube had a fluorescence spot that was flashing. The flashes were timed with the discharge that went through the tube. This was an unexpected event because, based on what was known, the cathode rays should have been absorbed by the air before they reached the sheet. This means that the florescence was caused by something else. Röntgen called this unknown thing X. Upon this discovery, Röntgen investigated this unknown X using several different experiments. After some years later, he published several papers [4,5,6] on what he eventually called x-rays. His research gave the scientific community some of the basic understandings of x-rays [3]. The research also included some applications of x-rays, such as taking pictures of his wife's hand that show the bones, as shown in Figure 2.



Figure 2: Picture of Röntgen's wife's hand. This is the result of placing her hand in front of an x-ray source. A photographic paper was placed on the other side of the hand. Figure taken from Ref [7].

#### 1.1.2. Laue's Discovery

Max von Laue became interested in the research using x-rays in 1912. In particular, he had an interest in the passage of short waves through a crystal. It was known that x-rays have short waves at a value somewhere between  $10^{-10}$  and  $10^{-9}$  cm and the lattice distance between layers of the crystal are in the order of  $10^{-8}$  cm [8]. After a conversation with Paul Ewald in 1912, Laue decided to design an experiment to gain understanding the relationship between x-rays and crystals. To start, he partnered up with Walter Friedrich and Paul

Knipping. They designed an experiment together using very basic equipment. Copper sulphate was used to serve as the crystal and it was placed inside a lead box with a hole for x-rays to enter. A photographic plate was placed between the x-ray source and the crystal in hope of seeing some diffraction pattern [3]. Nothing appeared on the plates and they responded by placing photographic plate all around the crystal. This change in the set-up produced blurry spots that appeared on the plate behind the crystal. With the knowledge of where there would be spots, they designed the set-up to get a clearer image behind the crystal which is shown in Figure 3. The resulting set-up is shown in Figure 4. To further provide evidences, they used powdered copper to show that crystal shape is important in producing this result. Powdered copper does not have a structure with a defined lattice distance. Laue's discovery was evidence that the crystal acts as a diffraction grating. A diffraction grating is a periodic array of slits that waves can travel through. A wave traveling through the grating is split into a set of waves that will interfere with each other. The interference will produce positions of maximum and minimum intensity. If the distance between the slits is on the order of the wavelength, the maximum and minima will be easily resolved. These discoveries led Laue to earn the Nobel Prize in Physics in 1914 [9].

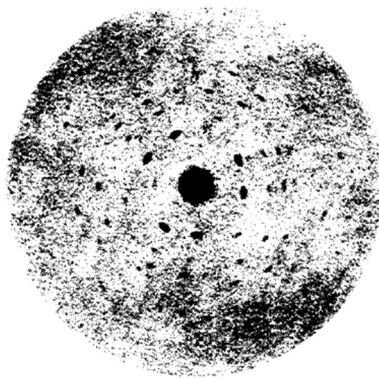


Figure 3: Laue, Friedrich, and Knipping's first successful image. Copper Sulphate was placed inside a lead box with a hole for x-rays to enter. The image appeared on a photographic plate behind the sample. The black blobs are the spots that are created by diffraction. Figure taken from Ref [9].

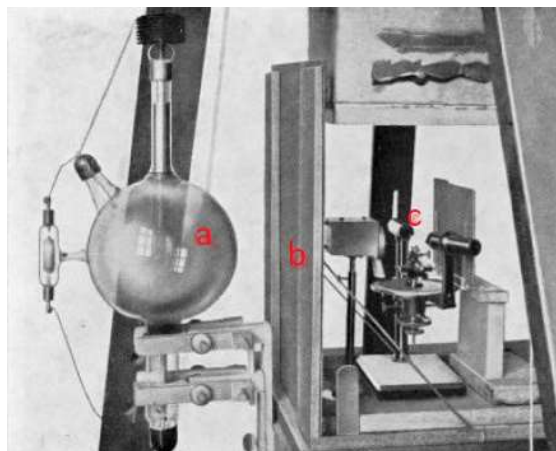


Figure 4: Picture of Laue, Friedrich, and Knipping's x-ray diffraction apparatus. The x-ray source is produced in the glass blub (a) and enters a hole in the metal shield (b). The crystal (c) stands between the photographic paper and the source. Figure taken from Ref [3].

### 1.1.3. X-Ray Diffraction (XRD) Development

After Laue's discovery, W.H Bragg and W.L. Bragg decided to look into the analysis of single crystals. They developed an instrument, which they named an x-ray spectrometer, to gain some reflection data of x-rays produced from a palladium target targeted at some salt rock [10]. The goal of the setup is to use Laue's discovery and Bragg's Law, explained later, to confirm the wavelength of various x-ray sources and the arrangement of single crystals.

Bragg first setup of the x-ray spectrometer is shown in Figure 5. The x-ray source was enclosed in a box coated with lead. The box had a fine slit on one side allowing rays to exit parallel to the instrument's axis. The rays then passed through another slit that allowed the adjustment of the width. The crystal sample was positioned in the pathway of the x-ray. It was mounted onto a table that was rotatable. This allowed the angle between the rays and the parallel surface of the sample to be adjustable. The reflected x-rays passed through a slit to isolate the reflected rays. The rays then entered a chamber filled with gas, usually  $\text{SO}_4$ , that absorbed them. The intensity of the rays that were absorbed affected the ionization current. This basic instrument set the basic structure of the XRD setup.



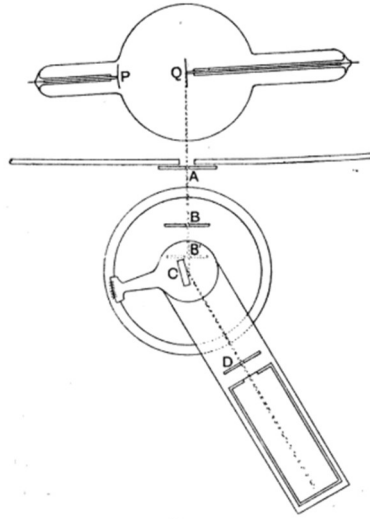


Figure 5: Bragg's first setup of the X-ray Spectrometer. The x-ray source was the bulb shown by P and Q. The rays exited the lead box through slit A. It then passed through slits B and reflected off the sample at C. The reflected rays passed through slit D into the chamber. Figure taken from Ref [10].

Bragg set up multiple experiments using this setup to gain an understanding of the structure of crystals and x-rays. They looked into various metals that had complex structure and were able to gain understanding of the actual structure [11,12]. They were also able to use the known crystal structure to determine the wavelength of various x-ray sources such as platinum, osmium, tungsten, and nickel [10]. They were also able to verify the relationship between the energy of the electron and the wavelength, i.e. Plank's constant. These experiments sparked many to experiment in this area. This led the father and son to receive a joint Nobel Prize in Physics 1915 [13].

XRD design has been modified over the century to improve the accuracy of the measured data. Several aspects have been redesigned to improve its function. One aspect is the x-ray source. One common method is using synchrotron radiation [14]. This method produces radiation when charged particles are accelerated in an orbit. The energy of the rays depends on the angular velocity and the orbit. This means that the user can change the variables to get any desired energy in the large radius.

Another important aspect that has been improved is the detector. There are a large variety in detector types and technologies that can and had been used in XRD [15]. With the new detectors, the measured data is based on individual counts rather than the current. This improves the accuracy and precision of the data. Other modifications of the detector focus on the range of the energy of the reflected rays that it detects. This is important in assuring the data that is measured depends on the reflected rays and not the background radiation.

## **1.2. XRD Thin Metal Film Research at Houghton College**

Thin films are essential to miniaturized electronics and are often used in integrated circuits. Understanding the texture and transformation of the thin metal is essential to improving the qualities of electronics. Houghton College has been conducting experimental research on thin metal films, using XRD to gain understanding of the texture transformation. The XRD experiments by Houghton College [16] have shown different aspects of the metal films that affect the texture transformations.

### **1.2.1. Thin Metal Films**

Metal films are considered thin when the thickness is much smaller than the width and length. The thickness is typically several hundred nanometers. Commonly used metals such as silver, copper, and nickel are face-centered cubic (FCC) crystals. This means that the atoms are arranged into a cube with one atom on each corner and one on the center of each face, as shown in Figure 6. These cubes are stacked in all three directions to create what is called a crystal.

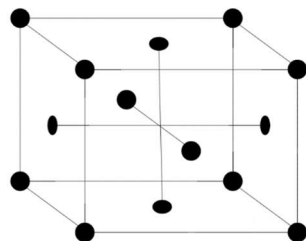


Figure 6: Diagram of the structure of a face-centered cubic. The black dots represent atoms. The black lines are included to show the cube shape.

The orientation of each cube within the crystal can be in any particular direction relative to the substrate. One way to describe the orientation is to use Miller Indices. Miller Indices define the normal vector of the plane of the cube that is parallel to the surface of the film. Figure 7 shows two common orientations and the corresponding normal vectors. For the (100) orientation, the normal vector points along one axis of the crystal. The (111) plane has a normal vector that has equal component in all three axes of the crystal. To get a better visualization of the two orientations, Figure 8 shows the top view of a face centered cubic crystal. Note that there is a difference in the arrangement of the layers.

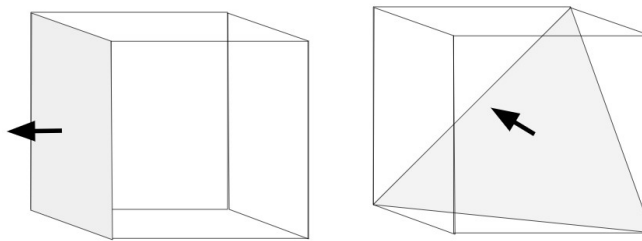


Figure 7: The normal planes of (100) on the left and (111) on the right. The cube shape is drawn to show cube structure of the crystal. The shaded plane and its corresponding arrow is the normal plane.

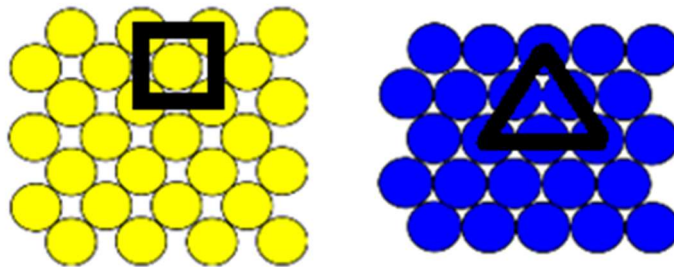


Figure 8: Top view of the arrangement of atoms for (100) and (111). The left is the arrangement for a (100) crystal. The right is the arrangement for a (111) crystal. The black lines are to outline the shaded region of the corresponding orientation in Figure 7.

The films for Houghton College research are commonly produced using Electron-Beam Physical Vapor Deposition (EBPVD) [17]. As shown in Figure 9, the target sample is heated when the electrons that are thermally emitted by the filament collide with the sample. To

assure that the electrons hit the top of the sample, to only melt the top layer, a magnet is added. The magnet allows the electrons travel in a circular path that is determined by the speed and magnitude of the charge. The material is warmed up to the point of evaporation. The atoms are evaporated and forms layers onto the substrate.

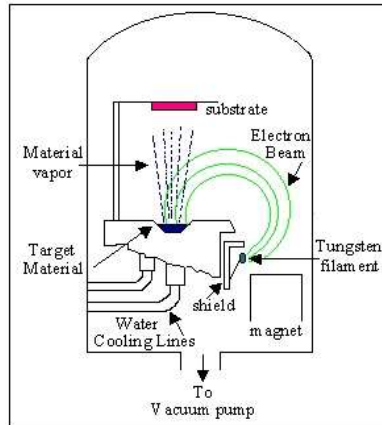


Figure 9: Diagram showing how an EBPVD creates a sample. The electron beam warms up the target material causing it to evaporate. Figure taken from Ref [18].

When an atom is absorbed onto the substrate, it is free to move along the substrate. The atoms will bind to each other such that it starts forming the FCC structure. After a small group of atoms bind together, their mobility is significantly diminished. This means that there will be groups of atoms throughout the sample that will form the FCC structure. These groups are called grains and will grow as more atoms are deposited. Grains are typically  $1\text{ }\mu\text{m}$  wide. The region between grains is called the grain boundary. The distance between these grains is determined by the temperature of the sample and the rate of deposition. Each grain will have a certain orientation that it is independent of the other grains. The variation of orientation is described as the texture of the film.

For an atom to cross grain boundaries, it must be able to overcome the activation energy. The activation energy refers to the energy difference between the occupied spot and the maximum energy level in the gap. When the metal film is annealed, the atoms are free to move around and are able to cross the grain boundaries. This means that the atoms will move back and forth between grains, spending more time in the grain with a lower energy state.

This causes certain grains to become larger at the expense of others until the length is about the same as the thickness of the grain. At this length, the boundary curvature has decreased enough such that the energy level of the particular grain is not significantly lowered by obtaining another atom. This type of grain growth is called normal grain growth.

The driving force of normal grain growth is to reduce boundary curvature. Grains with larger parameter to area is in a higher energy state than those with smaller ratio. It has no preference of the orientation choice [19]. This means that the texture of the film before and after the annealing process will be the same. This grain growth is shown in Figure 10a. There is another type of grain growth called abnormal grain growth. It is when the grain growth causes the texture of the film to change or transform. As shown in Figure 10b, a small percentage of the original grains take over the sample and change the texture. The final grains are also often larger than the ones found in normal grain growth.

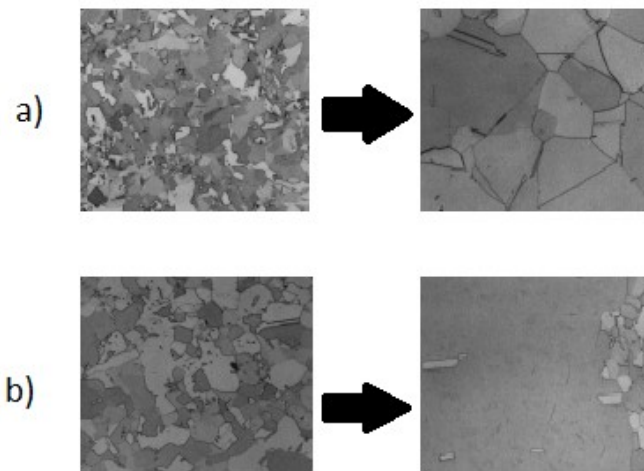


Figure 10: Images showing two general types of texture transformation. The grains are shown by the lines. Normal grain growth is shown in a) and abnormal grain growth is b). Figures taken from Ref [19].

One possible driving force for abnormal grain growth is minimization of stacking faults in the as-deposited grains. The layering position shown in Figure 11a is an example of the lowest state arrangement for three layers (A, B, C). For an FCC crystal, the arrangement of layers that follows the pattern of A, B, C arrangement will be in the lowest energy state. However, the energy state for a layer to be arranged in the incorrect arrangement once is

only slightly higher. Figure 11b shows an example of what is called a twin boundary. The twin boundary in this example is the second A arrangement layer because that is where the lowest energy state pattern was broken. The energy state difference between Figure 11b and Figure 11a is called the stacking fault energy. The overall energy state of the grain with the twin boundary is higher than the one without it.

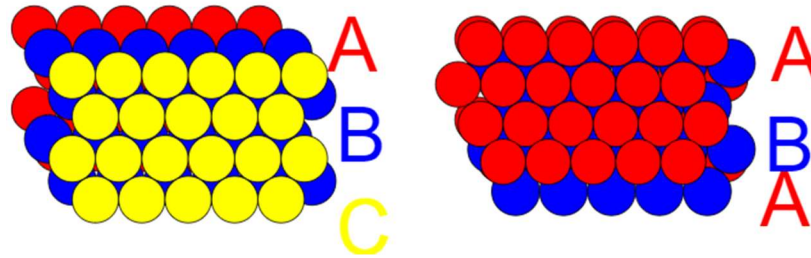


Figure 11: Diagram showing the formation of twin boundary. Each colored layer represents different arrangement of a layer of atoms. The left shows the lowest energy ordering of A, B, C. On the right, the third layer is on position A rather than C. This is a twin boundary layer.

### 1.2.2. Driving Force of Texture Transformation Research

At Houghton College, there has been research completed on silver thin films [16]. It has been found that there is a texture transformation that occurs during the annealing process. When silver films were deposited, they had a strong (111) texture. Once the samples were annealed, it was found that they sometimes transformed to a strong (100) texture. Figure 12 shows the texture of a set of silver films after they had been annealed at Cornell University. If the thickness of the film is larger than approximately  $1\ \mu\text{m}$ , there is an obvious texture transformation. Scanning Electron Microscopy also found that the grains were significantly larger than the thickness of the film. To explain this texture transformation caused by abnormal grain growth, a driving force has to be determined. These findings brought the focus of the research to the driving force.

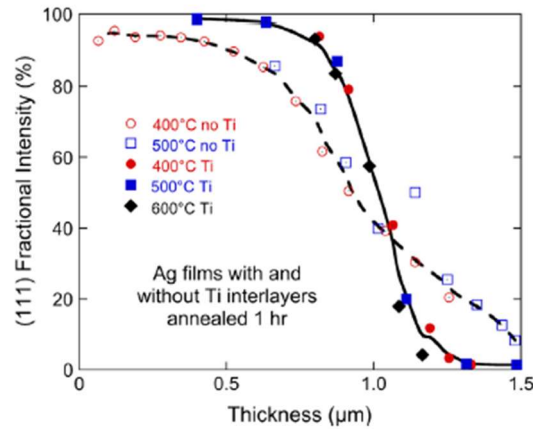


Figure 12: Graph of the fraction of the film that is in the (111) orientation. The sample had been annealed and for thicker samples, the texture is a strong (100). Figure taken from [16].

One aspect of the driving force research focuses on the effects of nanotwins. Nanotwins refers to a set of twin boundaries in a crystal with a separation distance on the order of nanometers. Twin boundaries are formed in the (111) plane. Since the (111) plane is slanted relative to the (100), the nanotwins created in (100) oriented grains are slanted. The nanotwins in (111) grains are parallel, as shown in Figure 13. As the grain grows, the nanotwins created in the (100) grains can be terminated once the twin boundary reaches the surface. On the other hand, the nanotwins in the (111) grains can never be terminated because they run parallel to the substrate surface. This means that the grain growth of the (100) grains will result in a larger drop in energy state than for the (111) grains. This causes the atoms to prefer the (100) grain and to transform the texture. Houghton College and Cornell University had done research in understanding the nanotwin and texture transformation [20,21].

The experiments included looking into effect of deposition speed on the texture transformation. Looking into this effect, three Ag samples were created at three different deposition speed, 10 Å/sec, 40 Å/sec, and 100 Å/sec. The samples were annealed for two hours. The final texture recorded using the XRD at Cornell University are recorded in Figure 14. It is obvious that the lower deposition speed resulted in less texture transformation than

it did for the faster deposition speed. There are still research needs to be completed to gain more understanding of the driving force.

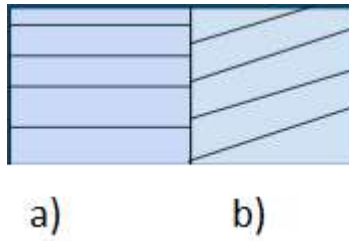


Figure 13: Diagram showing the difference of the (100) and (111) nanotwins. The black lines represent the twin boundaries. On the left (a) is the (111) grain with twins parallel to the substrate. On the right (b) is the (100) grain with slanted twins.

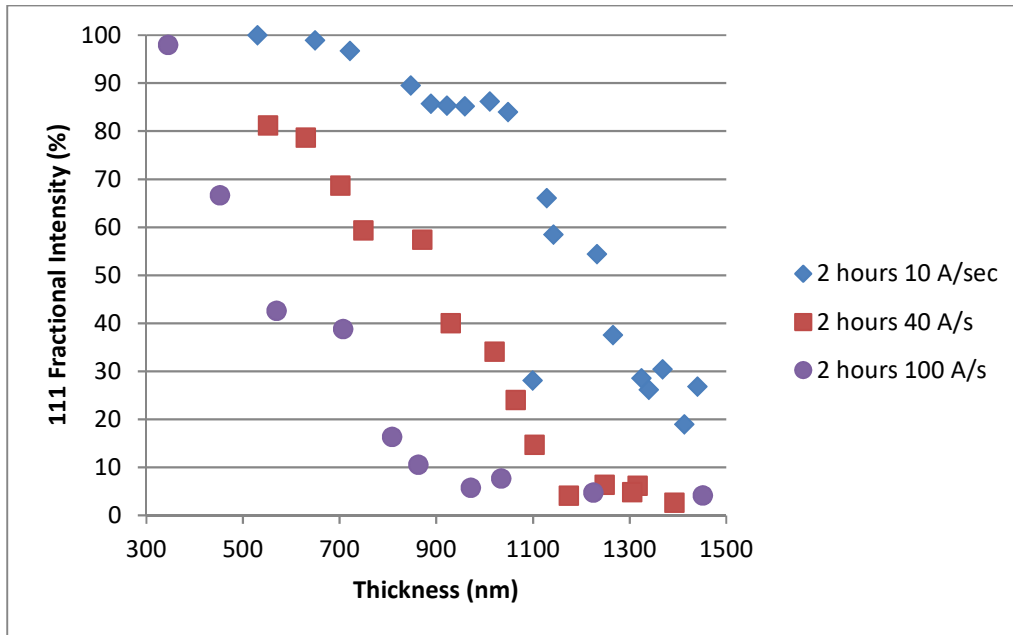


Figure 14: Fractional integrated intensity of (111) versus thickness for Ag films. Three films were deposited at different speed of 10 Å/sec (blue), 40 Å/sec (red), and 100 Å/sec (purple). The samples were annealed for 2 hours at 200°C. Figure taken from [20].

### 1.2.3. XRD at Houghton College

To further the research of texture transformation at Houghton College, an XRD under construction [22,23,24]. Texture data of thin metal films can be completed at Houghton



College rather than Cornell University. This allows data to be collected more often and gives the researchers freedom to obtain the needed data. Currently, modifications are being completed. The modifications are aimed to provide reproduceable data and reducing any safety hazards. Once this goal is achieved, the XRD will be used to improve the texture transformation research.

## Chapter 2

### THEORY

The XRD technique uses a symmetric  $\theta/2\theta$  arrangement. This means a collimated beam of x-rays with wavelength  $\lambda$  scatters off a crystalline sample toward a detector positioned at an angle  $\theta$  to the sample surface plane. The angle between the x-ray source and the detector is  $2\theta$ . Using Bragg's law, the measured intensity and the angles can be related to the texture of the film.

#### **2.1. X-ray Production**

X-rays are produced when electrons collide with a metal target. There are two general processes that produce x-rays. The first deals with the loss of kinetic energy due to collision between atoms and is called the bremsstrahlung x-ray. The second type is produced when the electron knocks a core electron out of an atom. This is called the characteristic x-ray. Characteristic x-rays are useful for XRD because the energy and wavelength of the x-ray is known.

##### **2.1.1. Bremsstrahlung x-ray**

When the electron approaches an atom, it interacts with the atomic nucleus, causing it to lose energy and change its direction of motion. [25]. Conservation of energy states that the energy loss by the atomic nucleus must be converted to another form of energy. The energy is converted to an x-ray. Figure 15 shows the electron passing through the atom and the x-ray produced. As shown in Figure 16, the energy of the emitted x-ray is distributed within the range based on the energy of the atomic nucleus. The maximum is due to the fact that the x-ray cannot have more energy than the energy of the incoming electron. Note that at very low energy, there is a very low count. This is due to the fact that low energy x-rays cannot escape the target material easily. Between these two extremes, there is a larger count at lower energy compared to higher energy. This is due to the fact that the electron will still have some kinetic energy after an incident and will continue to travel through the sample. Note that there are two large peaks. These peaks represent the characteristic x-rays.

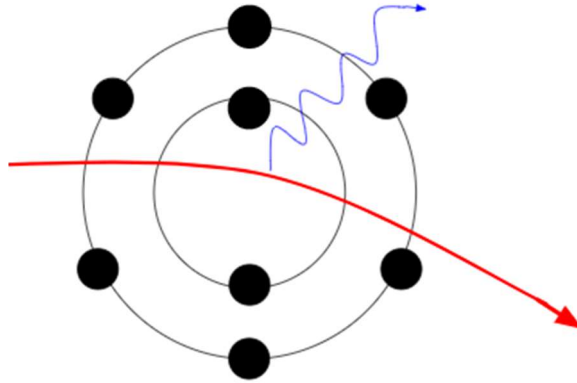


Figure 15: Diagram showing how a Bremsstrahlung x-ray is produced. Two orbits of electrons are shown as black circles. The red line represents the electron pathway and the produced x-ray is shown as the blue line.

### 2.1.2. Characteristic X-ray

There are two sharp peaks shown in Figure 16. These sharp peaks are a result of another method of producing an x-ray called the characteristic x-rays. There are two steps of producing the x-rays. In the first step, an electron collides with an atom and knocks off a core electron, as shown in Figure 17. This leaves an empty energy level that a higher-level electron could drop into, as shown in Figure 18. When this happens, it loses energy in the form of an x-ray. The energy of the emitted x-ray is equal to the energy difference of the two energy levels that the electron moved between. Looking at the sharp peaks in Figure 16, the two peaks are correlated to a specific drop in energy.

## 2.2. Wave interference

X-rays are a type of electromagnetic wave. They correspond to an energy level drop. This energy can be written in terms of wavelength:

$$E = \frac{hc}{\lambda} \quad (1)$$

where  $h$  is the plank's constant,  $c$  is the speed of light, and  $\lambda$  is the wavelength. They behave like a traveling electromagnetic wave which can be represented by a sine function. In general, an x-ray wave can be written as

$$E = E_0 \sin(kx - \omega t) \quad (2)$$

where  $E$  is the electric field of the x-ray beam,  $E_0$  is the amplitude,  $k$  is the wave number,  $x$  is the wave front position,  $t$  is the time, and  $\omega$  is the angular frequency. The superposition principle states that, when 2 or more traveling waves are moving, the resultant wave is the sum of the discrete individual waves. Consider two waves of equal magnitude, traveling in the same direction:

$$E_1 = E_0 \sin(kx - \omega t) \quad (3)$$

and

$$E_2 = E_0 \sin(kx - \omega t + \phi) \quad (4)$$

where  $\phi$  is the relative phase shift. The two waves will interfere with each other and produce a resultant wave of

$$E = 2E_0 \cos\left(\frac{\phi}{2}\right) \sin\left(kx - \omega t + \frac{\phi}{2}\right). \quad (5)$$

Noting that the phase shift arises when the two waves travel different distances, the phase shift can be written as

$$\phi = k\Delta x, \quad (6)$$

where  $\Delta x$  is the path length difference. Therefore, the resultant wave can be written as

$$E = 2E_0 \cos\left(\frac{k\Delta x}{2}\right) \sin\left(kx - \omega t + \frac{k\Delta x}{2}\right). \quad (7)$$

Note that

$$\left| 2E_0 \cos\left(\frac{k\Delta x}{2}\right) \right| \quad (8)$$

is the amplitude of the resultant wave. The maximum amplitude occurs when the cosine term equals to 1 or -1. This means that for maximum amplitude, the path length difference is

$$\Delta x = \frac{n2\pi}{k} = n\lambda, \quad (9)$$

where  $n$  is integer and  $\lambda$  is the wavelength of the x-ray. This results in the maximum constructive interference, as shown in Figure 19. The minimum constructive interference, more commonly known as destructive interference, occurs when

$$\Delta x = \frac{m\pi}{k} = \frac{m\lambda}{2} \quad (10)$$

where  $m$  is an odd integer, as shown in Figure 20. Note that path length distances other than the values shown in Equation 9 and Equation 10 will result in some constructive interference, as shown in Figure 21.

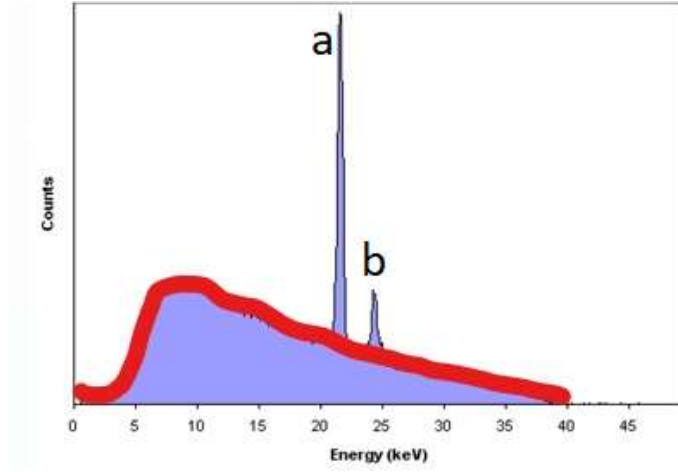


Figure 16: Graph of the photon counts for a spectrum of energies of x-rays produced. This data was produced from an experiment where 40 kV x-rays collide with a Ag target. The red line shows the Bremsstrahlung background. The peaks at a) and b) shown are the results of characteristic x-rays of energies 21 keV and 24 keV. Graph taken from Ref [26].

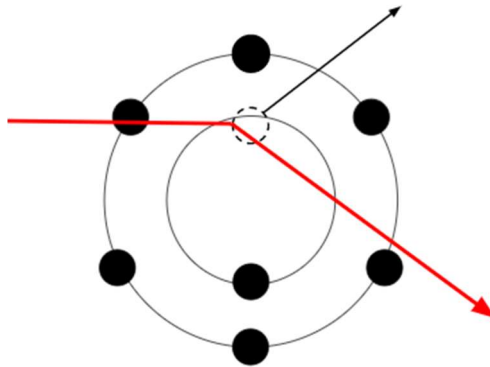


Figure 17: Diagram of the first step of producing a characteristic x-ray. The red line represents the electron pathway to colliding with a core electron. The dashed line shows the empty energy level that occurs when the core electron leaves as shown by the black arrow.

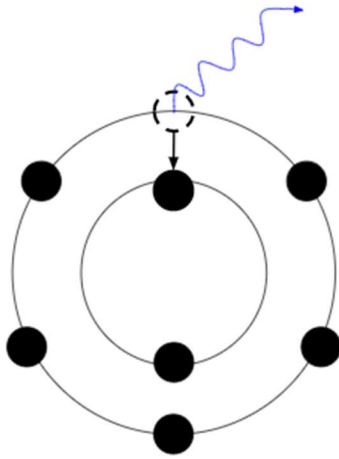


Figure 18: Diagram of the second step of producing a characteristic x-ray. An electron on a higher energy level moves to the empty energy level, as shown by the black arrow, emitting a photon.

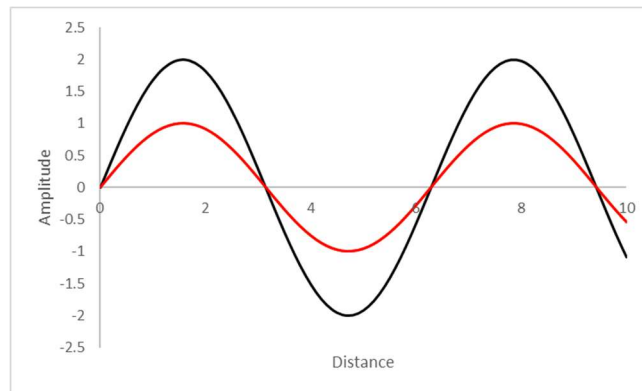


Figure 19: Example graph of constructive interference. The red line is the wave function of the two original waves and the black line is the resultant. As seen the resultant wave has an amplitude that is twice as big as the individual waves.

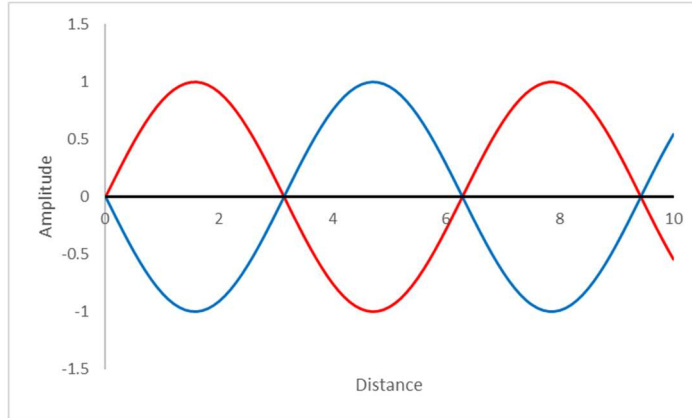


Figure 20: Example graph of deconstructive interference. Red and blue lines are the two original wave functions. The resultant is shown in the black line. Note that the resultant is a wave with the amplitude of zero.

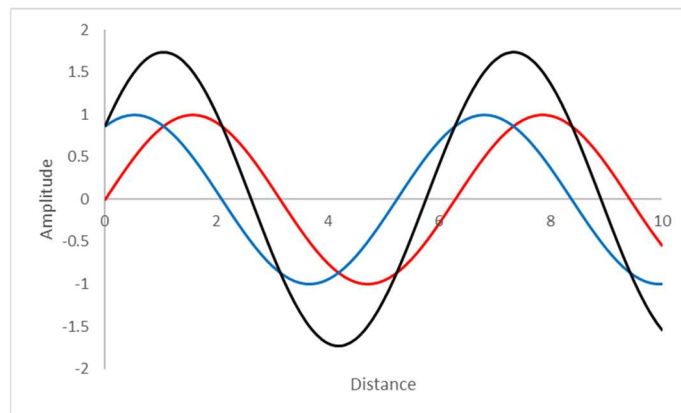


Figure 21: An example of a general wave interference. Red and blue lines are the original wave functions. The resultant is the black line.

### 2.3. *Bragg's Law*

When an x-ray reaches the target, there is a probability that it will interact with an atom in its path. Each x-ray will interact with different atoms. It is important to note that some will travel further into the sample before interacting. Figure 22 represents a cross-section view of the thin film, with the surface at the top and the x-rays interacting and diffracting. The x-rays are initially in phase but, once the diffraction occurs, some of the x-rays have to travel further which results in a phase shift. As explained in Section 2.2, in order to achieve

constructive interference between the outgoing x-rays, the path length difference must be an integer multiple of a wavelength. Figure 23 shows one half of the extra distance of

$$2d \sin(\theta) \quad (11)$$

that the second set of waves has to travel. Using the idea of the extra length, Bragg's law sets up the condition for constructive interference of

$$2d \sin(\theta) = n\lambda, \quad (12)$$

with  $n$  as any integer,  $d$  is the lattice distance between layers, and  $\theta$  is the angle between the incident x-ray beam and the sample surface, as shown in Figure 22. If constructive interference occurs at a certain incident angles, the lattice distance between the layers,  $d$ , can be calculated using Equation 12. Bragg's law is useful in explaining some effects that occurs in an intensity vs 2-theta plot.

The amplitude of the electric field of two interfering waves varies sinusoidally with the path length difference, as seen in Equation 8. The x-ray intensity is proportional to the square of the amplitude. Therefore, the x-ray intensity from reflections off two crystal layers would vary gradually between background and peak intensity, when plotted against 2-theta. However, real samples contain hundreds or thousands of layers, each of which produces x-ray reflections. If the incident angle is even slightly off from the Bragg angle, every plane will have a complementary plane where the reflected x-rays will have a large enough path difference to cause the x-rays to destructively interfere. Therefore, the crystal will not produce any reflected x-ray intensity at that angle. However, for incident angles that corresponds exactly to the Bragg's law, any layer will have a layer below it where the reflected x-rays will constructively interference. Therefore, all interference will be constructive at that angle. As the number of crystal layers approaches infinity, the width of the intensity peaks would become infinity thin (ignoring any other contributions to peak width). The overall peak will be large enough to be a noticeable peak.



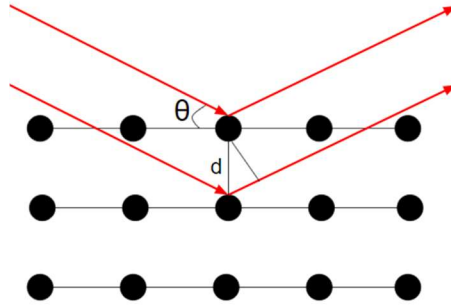


Figure 22: Diagram demonstrating the usage of Bragg's Law. The layers of atoms are shown by the black circles. The x-rays travel according to the red arrows. Using the measured  $\theta$ , the lattice distance ( $d$ ) can be calculated.

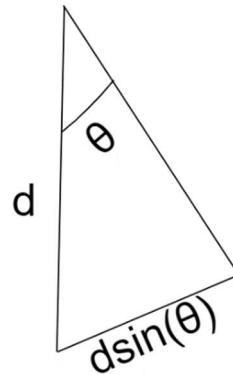


Figure 23: The right triangle found in Figure 22. The unlabeled side of the triangle is the wave front. Using trigonometry, the extra distance that the outgoing x-rays have to travel can be calculated.

#### 2.4. Correction Factor

In XRD, a collimated beam of x-rays with wavelength  $\lambda$  scatters off a crystalline sample toward a detector positioned at an angle  $\theta$  to the sample surface plane. The intensity,  $I$ , of the x-ray detected depends on the spacing,  $d$ , between atomic planes parallel to the sample surface plane. The relationship between the spacing,  $d$ , and the angle,  $\theta$ , can be determined by Equation 12. If the sample is polycrystalline, the intensity will also depend on the percentage of the sample that has the appropriate crystal plane spacing. Since, each orientation of a crystal has a different plane spacing, XRD can determine the percentage of

each orientation. The measured intensity depends on a number of factors. To focus on the orientation factor, the intensity needs to be corrected to remove the effects of the other factors. Each factor is described in the following sections.

#### 2.4.1. Structure Factor

The first factor that needs to be considered is the structure of the crystal. Starting with the traveling wave, it can be written as a complex exponential:

$$\psi = Ae^{i\phi} = Ae^{i(\vec{k} \cdot \vec{x} - \omega t)} \quad (13)$$

where  $A$  is the amplitude,  $\phi$  is the phase of the wave,  $\vec{k}$  is the wave vector,  $\vec{x}$  is the position in space, and  $t$  is the time. When considering a collimated beam of x-rays scattering elastically off a simple cubic crystal, the wave numbers of the x-rays before and after the interaction with the crystal are all equal. Consider two x-rays that interacted with different atoms. One x-ray scatters off an atom located at the origin, at time  $t = 0$ . The other x-ray scatters off an atom located at  $\vec{x}_2$ . Since the initial phases of both x-rays are equal and the second x-ray traveled further to the detector after scattering, it picked up an additional phase of  $-\vec{k}_f \cdot \vec{x}_2$ . Using Equation 13, the resulting final wavefunction for that x-ray is

$$\psi_{2f} = Ae^{i(0 + \vec{k}_i \cdot \vec{x}_2 - \vec{k}_f \cdot \vec{x}_2)} = Ae^{-i(\vec{q} \cdot \vec{x}_2)} \quad (14)$$

where  $\vec{q} \equiv \vec{k}_f - \vec{k}_i$  is called the scattering vector. Looking back to the first x-ray, Equation 14 still applies since  $\vec{x}_2 = 0$ . Expanding on the two x-rays example to the general wavefunction for any of the scattered x-ray, the wavefunction can be written as

$$\psi_{jf} = Ae^{-i(\vec{q} \cdot \vec{x}_j)}. \quad (15)$$

Considering all the outgoing x-rays, the overall wavefunction is a linear combination of Equation 15:

$$\psi = \sum_{j=1}^N f_j e^{-i\vec{q} \cdot \vec{R}_j} \quad (16)$$

where  $N$  is the number of scattering atoms,  $f_j$  is the atomic form factor. Looking back to the scattering factor, using basic trigonometry similar to Figure 23,  $\vec{q}$  can be written as

$$\vec{q} = 2\kappa \sin \theta \hat{n}. \quad (17)$$

The normal vector can be written in terms of the Miller indices and the unit vectors of the crystal lattice. Using  $h, k, l$  as the Miller indices and  $\hat{a}, \hat{b}, \hat{c}$  as the unit vectors of the crystal lattice,

$$\vec{q} = 2\kappa \sin \theta \left[ \frac{h\hat{a} + k\hat{b} + l\hat{c}}{\sqrt{h^2 + k^2 + l^2}} \right]. \quad (18)$$

Rewriting the position vector of an x-ray in terms of the unit vectors, it becomes

$$\vec{x}_j = a(x_j\hat{a} + y_j\hat{b} + z_j\hat{c}) \quad (19)$$

where  $a$  is the lattice constant and  $x_j, y_j, z_j$  are the distances in unit of  $a$ . Using Equation 18 and Equation 19,

$$\vec{q} \cdot \vec{x}_j = (2\kappa \sin \theta) a \left[ \frac{hx_j + ky_j + lz_j}{\sqrt{h^2 + k^2 + l^2}} \right]. \quad (20)$$

Using Equation 18 and  $d = \frac{a}{\sqrt{h^2 + k^2 + l^2}}$ , Equation 20 can be rewritten as

$$\vec{q} \cdot \vec{x}_j = 2\pi n(hx_j + ky_j + lz_j). \quad (21)$$

Therefore, the overall scattered wavefunction becomes

$$\psi_f = \left( \frac{N}{m} \right) \left[ f \sum_{j=1}^m e^{-i2\pi(hx_j + ky_j + lz_j)} \right] \equiv \left( \frac{N}{m} \right) f F_{hkl}. \quad (22)$$

where  $F_{hkl}$  is called the structure factor and  $\frac{N}{m}$  is the number of cells. Note that  $f$  has been pulled out of the sum since  $f$  is identical for all the atoms. For an FCC crystal, there is an atom at the corner which can be designated as the origin and three face atoms. Using this structure, the structure factor can be rewritten as

$$F_{hkl} = f \left( e^{-i2\pi(0)} + e^{-i2\pi(\frac{h}{2}+\frac{k}{2})} + e^{-i2\pi(\frac{h}{2}+\frac{l}{2})} + e^{-i2\pi(\frac{k}{2}+\frac{l}{2})} \right) \quad (23)$$

For the two orientations used in the study, the structure factor only differs by the atomic form factor. Considering the effect of the structure factor on the wavefunction, it has an effect on the intensity. Since intensity is proportional to the square of the wavefunction,

$$I \propto |F_{hkl}|^2. \quad (24)$$

#### 2.4.2. Atomic Form Factor

The atomic form factor accounts for the interferences from rays scattering off different regions of the electron cloud. This is the result of fact that the wavelength is on the order of the atomic radius. Since the electron cloud is continuous, sum of  $f$  is the integral over all space. The integral is difficult but it can be shown that

$$f \approx \sum_{i=1}^4 a_i e^{-b_i \left(\frac{q}{4\pi}\right)^2} + c = \sum_{i=1}^4 a_i e^{-b_i \left(\frac{\sin\theta}{\lambda}\right)^2} + c \quad (25)$$

where  $a_i$ ,  $b_i$ , and  $c$  are calculated from experiments.

#### 2.4.3. Lorentz Factor

Another factor that needs to be accounted for is the theta-dependence of the time that the crystal spends near the Bragg angle [26]. A vector diagram for  $\vec{k}_i$  and  $\vec{k}_f$ , the incoming and outgoing wave vector, can be drawn to satisfy Bragg's law, as shown in Figure 24. Since the magnitudes of the wave vector, wave number, are determined by the x-ray source, they are constant. Therefore, the circle in Figure 24 represents all the possible values of  $\vec{k}_f$ . For a symmetric  $\theta/2\theta$  arrangement,  $\vec{q}$  points normal to the sample surface. The sample is rotated, to change the scattering angle, at a constant velocity, with respect to the incident x-ray's direction. Therefore, the sample may be represented by a rotating  $\vec{q}_b$  at a constant angular velocity of  $\omega$ . Note that  $\vec{q}_b$  points in the direction of the scattering angle with magnitude determined by Bragg's law. Using the fact that  $\vec{q}_b$  has a constant length that is determined by Bragg's law, there is an angle where the arc formed by the rotation of  $\vec{q}_b$  will cross the circle shown in Figure 24. It is important to note that, for a real crystal, constructive inference will occur even when the angle is slightly off. Depending on the angular velocity of  $\vec{q}_b$ , the area of

the intensity peak will change. This means that the intensity area is inversely proportional to the  $\vec{k}_f$  component of the velocity of  $\vec{q}_b$ . Since the correction is focused on the effect on the changing  $\theta$ , the angular velocity can be ignored. At the Bragg angle, it can be said that

$$\int I d\theta \propto \frac{1}{\vec{q} \cos(\varphi)}. \quad (26)$$

where  $\varphi$  is the angle between the velocity vector at point P and  $\vec{k}_f$  and  $\int I d\theta$  is the area of the intensity. Using the trigonometry and the triangle of Figure 24, Figure 25 shows that  $\varphi$  is equal to  $\theta$ . Now using law of sines, it can be shown that

$$\vec{q}_b \cos(\theta) = \vec{k} \sin(2\theta). \quad (27)$$

Therefore, the angular dependence of the integrated intensity due to the Lorentz factor can be written as

$$\int I d\theta \propto \frac{1}{\sin(2\theta)}. \quad (28)$$

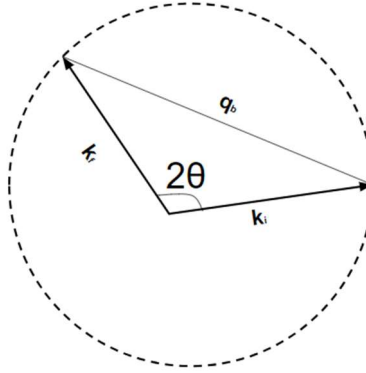


Figure 24: Vector diagram that satisfy Equation 12. The two wave vectors are shown. The circle represents the range of  $k_f$ .

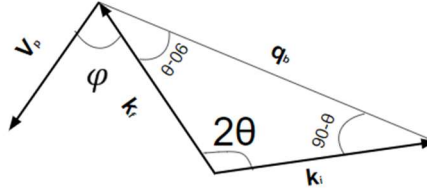


Figure 25: Diagram showing the triangle of Figure 24 and the velocity vector. The triangle allows the angles to be calculated.

#### 2.4.4. Attenuation Factor

Some x-rays will be absorbed as the beam travels through the film. This also needs to be accounted for. When the x-rays are absorbed, the intensity drops exponentially over the length. This drop can be described as

$$I = I_0 e^{-\mu l} \quad (29)$$

where  $\mu$  is the attenuation coefficient and  $l$  is the distance that the rays travel through the film. The attenuation coefficient is a value specific to the energy of the x-ray and the material that it is traveling through. Like as discussed in Section 232.3, the extra length,  $l$ , is

$$l = \frac{2z}{\sin\theta}. \quad (30)$$

However, each x-ray will interact with an atom in the pathway. This means some x-ray will interact with an atom while others will interact with a different atom which means that they will have different  $z$  and length travelled. Assuming that the probability of scattering is independent of the position, the intensity of x-rays scattered from all possible depths can be added up. Since there is a large number of x-rays, the sum can be approximated as an integral. Entering Equation 30 into Equation 29 and taking the integral over the total thickness of the film,  $t$ , gives the total intensity of

$$I = I_0 \int_0^t e^{-2\mu z/\sin\theta} dz. \quad (31)$$

Therefore, the angular dependence of the integrated intensity due to attenuation is

$$I \propto (1 - e^{-\frac{2\mu t}{\sin\theta}}). \quad (32)$$

#### 2.4.5. Polarization Factor

The last factor to consider is that the x-ray radiation is unpolarized [26]. This means that the radiation can be written as a combination of two light rays, one ray parallel to the plane formed by the rays and one ray perpendicular to the plane. With  $E_f$  being the electric field produced by the outgoing wave and  $E_i$  is the electric field of the incoming wave, it can be written that

$$E_f = (\hat{E}_i \cdot \hat{E}_f) E_i. \quad (33)$$

Calling the angle between  $\hat{E}_i$  and  $\hat{E}_f$   $\Phi$ , Equation 33 becomes

$$E_f = E_i \cos(\Phi). \quad (34)$$

The intensity is proportional to the square of  $\vec{E}$ . If the electric field of the x-ray is parallel to the plane formed by  $\vec{k}_i$  and  $\vec{k}_f$  then  $\vec{E}$  will rotate along with  $\vec{k}$ . Therefore  $\Phi = 2\theta$ . On the other hand, if the electric field is perpendicular to the plane, then  $\vec{E}$  does not change. Therefore  $\Phi = 0$ . Combining equal parts of both cases to get the total intensity,  $I_f$ , of

$$\frac{1}{2} I_i (\cos^2(2\theta) + 1). \quad (35)$$

Focusing on only the effect of  $\theta$ ,

$$I \propto (1 + \cos^2(2\theta)). \quad (36)$$

#### 2.4.6. Overall Correction

Putting together all the factors that needed to be accounted for gives the overall correction factor. Combining Equation 24, Equation 28, Equation 32, and Equation 36 the correction is written as

$$\int I d\theta \propto |F_{hkl}|^2 \frac{(1 + \cos^2 2\theta)}{\sin(2\theta)} (1 - e^{-2\mu t / \sin\theta}). \quad (37)$$

The measured intensity area divided by the correction gives the intensity area that only depends on the orientation of the film as shown:

$$[\int I d\theta]_{corrected} = \frac{\int I d\theta}{|F_{hkl}|^2 \frac{(1+\cos^2 2\theta)}{\sin(2\theta)} (1-e^{-2\mu t/\sin\theta})} . \quad (38)$$



## Chapter 3

### DESIGN AND MODIFICATIONS

#### 3.1. Overview

The XRD at Houghton College had been designed and built. It is designed to be a semicircle table with two movable arms. One arm rotates the sample while the other rotates the detector. The arms are moved using Lin Engineering 101411 stepper motors controlled by LabVIEW. The x-ray source is produced by a Philips-Norelco that is powered by a Hitek 1000 series 40-kV power supply. The XRD had been modified to improve the function and safety features.

#### 3.2. Basic Design

##### 3.2.1. Table

Figure 26 shows the basic set up of the XRD built upon a 1.83x1.22 m table. The x-ray source is on the right and is targeted at the sample. There are two arms that are both movable using Lin Engineering 101411 stepper motors. The motors were modified by adding a sleeve with thickness of 1.53 mm. An o-ring with the radius of 3.81 mm was added on the sleeve. This assures a smooth round surface for the motor. A LabVIEW program controls the motors such that the arms rotate along a radius of 58.60 cm. One arm rotates the sample to change the angle that the x-rays hits the sample. The other arm moves the detector along the table. Note that the sample arm rotation angle corresponds to the  $\theta$  in Bragg's law. The detector arm angle is rotated to  $2\theta$  according to Bragg's law. The motors are positioned with the shaft hanging over the edge of the semicircle of only 6.35 mm. The shafts are horizontal to the semicircle such that they rotate along the surface. The precision due to the motor is given by:

$$\left(\frac{0-rin}{200\ steps}\right)\left(\frac{3.81\ mm\ semicircle\ cycle}{586\ mm\ o-ri\ cycle}\right)\left(\frac{360^\circ}{1\ cycle}\right) = 0.012\ \frac{degree}{step}. \quad (39)$$

The picture of the actual table is shown in Figure 27.

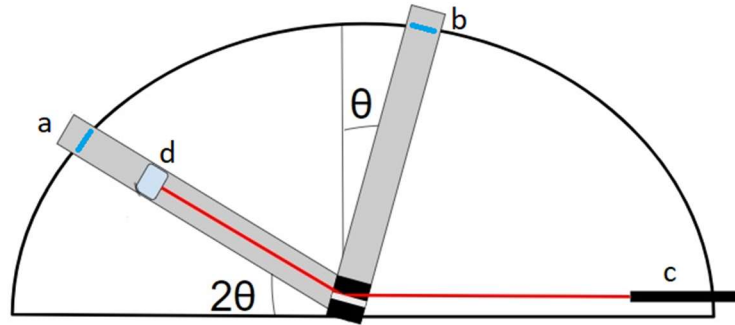


Figure 26: Diagram of the basic design of the. Arm (a) moves the detector while arm (b) rotates the sample. Red line indicates the x-ray beam coming from the source (c). The x-ray diffracts off the sample to the detector (d).

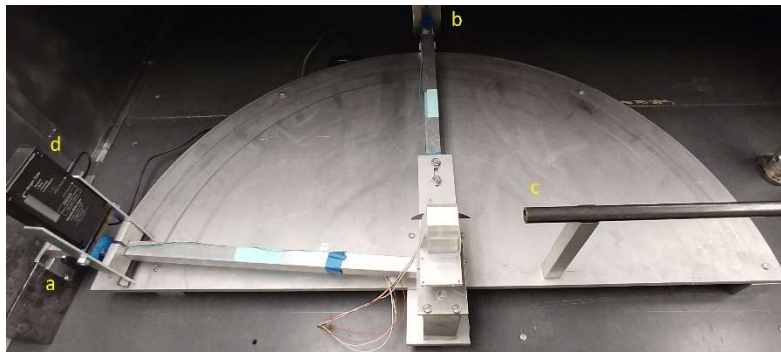


Figure 27: Figure of the actual table. The two arms, x-ray source, and detector are labeled according to Figure 26.

### 3.2.2. X-ray Production

A 12 V battery alongside a variable resistor is connected in series with a filament, as shown in Figure 28. The circuit is connected to a 40 kV power supply to float the circuit at -40 kV. There is also a copper target that is grounded, producing a voltage difference between the filament and the target. The copper target and filament are shown in Figure 29. This voltage difference causes electrons to accelerate toward the target. The interaction between the electrons and the copper produces x-rays, as discussed in Section 2.1.

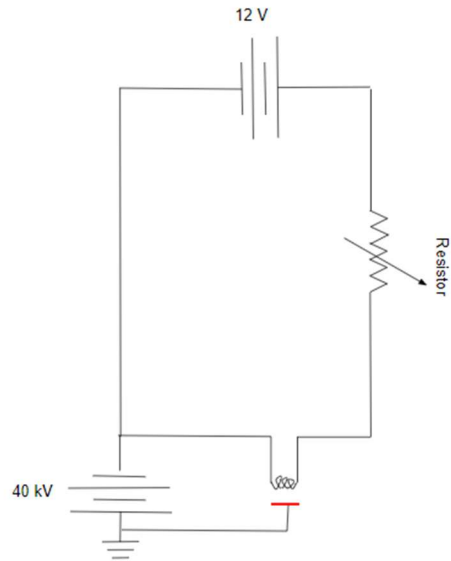


Figure 28: Diagram of the circuit. Electrons emit from the filament and accelerate toward the copper target (red line). This interaction produces x-rays.



Figure 29: Figure of the copper target and filament. This is included in the circuit that produces x-rays.

### 3.3. *LabVIEW Programs*

Two LabVIEW programs control the motors and the position of the two arms. They are both designed for different types of tests. The data from the detector are recorded in LoggerPro.

### 3.3.1. Long Scan

The Long Scan program was designed and modified to collect data while changing  $\theta$  and  $2\theta$  over a desired range. The user enters in the target end  $2\theta$ , how often the arm will scan, and the amount of time the arm will spend at each stop. The LabVIEW program will start with both arms at their “zero” position. It will move both motors every  $x$  seconds to change  $2\theta$  another  $y$  degree. The variables  $x$  and  $y$  are based on what the user entered. The program loops through this process until  $2\theta$  of the arm is at the desired target end  $2\theta$ . This provides a long scan over a range of  $\theta$  and  $2\theta$ .

### 3.3.2. Constant $\theta$

The Constant  $\theta$  program was designed as a calibration scan using a known  $2\theta$  peak. It was also designed to only scan at a set  $\theta$ . This program has two parts. The first takes the user desired  $\theta$  and  $2\theta$  and move the motors to the respective positions. The second part is the scanning part. This part is similar to the long scan discussed in 3.3.1. The difference is that this scan changes  $2\theta$  without changing  $\theta$ .

## 3.4. *Safety Features*

### 3.4.1. Plexiglass Box

A plexiglass box with a door was added to enclose the circuit. The box was designed to be as large as possible so that each component of the circuit can have room in the box. The dimensions of the box are 58.5 cm x 43.2 cm x 37.5 cm. To eliminate any metal that passes through the inside of the box to outside, the door was designed to not have a metal handle. Only two holes were drilled on the top. A small 1.3 cm hole allows the 40 kV power supply source to enter into the box. The larger 3.8 cm hole allows the filament chamber to fit inside the box. A switch was added to the side so that, when the door is opened, the power supply will automatically shut off. This serves as a safety off switch.

### 3.4.2. Steel Shielding

A 3.175 mm thick steel shielding surrounds the table to prevent any x-rays from escaping into the room. The shielding on the sides are mounted using a Steel angle bracket drilled to the table. For the side closest to the sample, there are hinges rather than angle brackets. This allows that side to be openable. A screw is added to both sides to keep the door closed when

needed. There is a stack of lead bricks that are placed in line with the x-ray source. This is to assure that outside the box, the radiation is below background.

## Chapter 4

### RESULTS AND DISCUSSION

#### **4.1. Testing the XRD**

##### 4.1.1. Set up

Using the constant  $\theta$  LabVIEW program as explained in 3.3.2, multiple scans were completed. With the knowledge that the sample contained Silicon (111), the scans were focused around the area of where  $2\theta = 69^\circ$ . The scans were set to vary  $2\theta$  from  $59^\circ$  to  $79^\circ$  and collect data every 10 seconds and increase  $2\theta$  by half degree. LoggerPro recorded the total count over the 10 seconds. The results were translated into Excel Sheet and graphed. The uncertainty in the count is based on  $\sqrt{\text{count}}$ . To determine the uncertainty in  $2\theta$ , a series of tests were completed to determine how quickly the count dropped as  $\theta$  increases.

##### 4.1.2. Results

Setting  $\theta$  to  $36^\circ$ , the scan was completed. The result is shown in Figure 30 and there is a peak at  $2\theta$  of  $70.5^\circ$ . This does not match the expected  $2\theta$  of  $72^\circ$  which indicates that the motors are not moving to the correct angles. Si peaks width depends mostly on the instrument. Since peaks collected has a small height, indicate that there is some error due to the alignment of the sample. However, the fact that there is a reproducible peak suggest that the set up was able to detect Silicon (111). This indicates that the XRD at Houghton College can measure the texture of the film. A scan setting  $\theta$  to  $35^\circ$  was also completed and there is a peak at  $2\theta$  of  $69.5^\circ$ , as shown in Figure 31. Again, like before, the  $2\theta$  was not where it was expected to be. It is also important to note that in both scans, the background noise is large. The  $35^\circ$  scan had higher count throughout the scan compared to the  $36^\circ$  scan. This along with the large noise suggests that the x-ray source is not producing a constant energy.

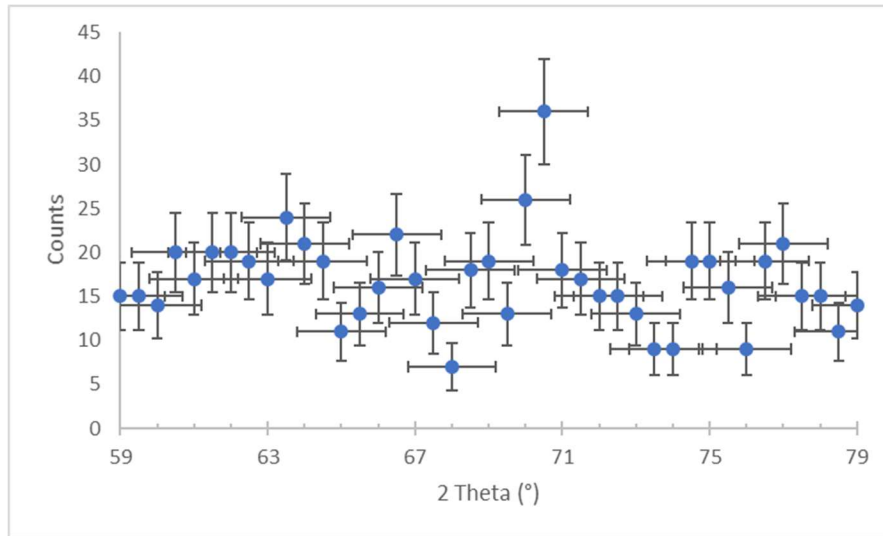


Figure 30: Radiation count vs 2-theta graph for constant theta of 36°. The test was completed using a of a Silicon wafer. There is an obvious peak at a  $2\theta$  value of 70.5°.

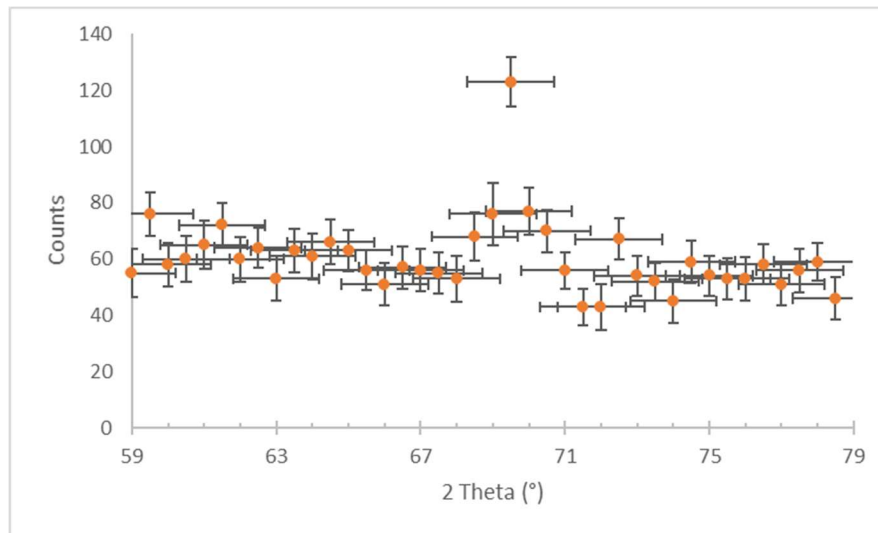


Figure 31: Radiation count vs 2-theta graph for constant theta of 35°. The test was completed using a of a Silicon wafer. There is an obvious peak at a  $2\theta$  value of 69.5°.

## **4.2. Future Plans**

### **4.2.1. Extra Safety Features**

The shielding around the table needs to be completed. The top needs to be screwed on to the edge bracket. Along with the completion of the box, interlocks are to be added. This will allow the power supply to automatically shut off if a plate of the box was removed.

To reduce chances of sparking in the box, a few measures need taken care of. The box needs to be cleaned on the inside with alcohol to prevent static energy storing on the walls of the box. Using a batter with smaller voltage can lessen the amount of energy loss across the resistor.

### **4.2.2. Improve the motor reproducibility**

There must be a way for LabVIEW to recalibrate the position once in a while. One method of achieving that is to place an LED every  $10^\circ$ . Placing a light sensor on each arm that would allow LabVIEW to correspond the correct position and the stepper motor's measured position.

### **4.2.3. Improve the radiation count**

To measure the x-ray energy, a second detector can be added. This one would be at a fixed point and will measure the count rate and determine if there are fluctuations during the scan. This can provide with explanation and allows us to account for the noise. Getting a detector that is energy resolved can reduce the background noise and focus on the larger intensity x-rays.



## References

- 
- [1] W. Crookes, *On Radiant Matter*. (Queen, Philadelphia, 1879).
  - [2] The Chicago Physician Who Understood the Paradox of Radiation (<http://www.zocalopublicsquare.org/2016/05/04/the-chicago-physician-who-understood-the-paradox-of-radiation/chronicles/who-we-were/>).
  - [3] P. Ewald, *Fifty Years Of X-Ray Diffraction*, (Published for the International Union of Crystallography by A. Oosthoek's Uitgeversmij, Utrecht, 1962) p. 31-56.
  - [4] W.C. Rontgen, *Science* **3**, 227 (1896).
  - [5] W.C. Rontgen, *Science* **3**, 726 (1896).
  - [6] W.C. Rontgen, *Science* **3**, 458 (1896).
  - [7] The hand of Mrs. Wilhelm Roentgen: the first X-ray image ([https://www.nlm.nih.gov/dreamanatomy/da\\_g\\_Z-1.html](https://www.nlm.nih.gov/dreamanatomy/da_g_Z-1.html)).
  - [8] M. Laue, *Journal of the Röntgen Society* **9**, 121 (1913).
  - [9] M. Laue, *Concerning the detection of X-ray interferences*, Nobel Lecture (Unpublished).
  - [10] W. H. Bragg and W. L. Bragg, *X-rays and Crystal Structure* (G. Bell and Sons, LTD., London, 1915).
  - [11] C.W Bunn, E.V Garner, W.L Bragg, *Mathematical and Physical Sciences* **189**, 39 (1947).
  - [12] W.L. Bragg, *Mathematical and Physical Sciences* **89**, 248 (1913).
  - [13] W. L. Bragg, *The diffraction of X-rays by crystals*, Nobel Lecture (Unpublished).
  - [14] J. Als-Nielsen, D. McMorrow, *Elements of Modern X-ray Physics* (John Wiley & Sons, 2011).
  - [15] Bruker.com (2018).
  - [16] S.P Baker, B. Hoffman, L. Timian, A. Silvernail, E.A Ellis, *Acta Materialia* **61**, 7121 (2013).
  - [17] H. Phillips, SRI Report (Houghton College, NY, 2016 unpublished).
  - [18] Gold Coated Glass Slides and Silicon Wafers (<https://www.azonano.com/article.aspx?ArticleID=3458>).
  - [19] S.B Lee, *Metallurgical and Materials Transactions* **31**, 981 (2000).
  - [20] J. Yuly, K. Flemington, P. Lashomb, B. Hoffman, SRI (Houghton College, NY, 2014 unpublished).
  - [21] B. Hoffman, N. Rogers, S. Olandt, D. Zhuravlev, S.P. Baker, SRI (Houghton College, NY, 2018 unpublished).
  - [22] A. Evans, Undergraduate Thesis (Houghton College, New York, 2013, unpublished).
  - [23] M. Kirkland, Undergraduate Thesis (Houghton College, New York, 2016, unpublished).
  - [24] J. Cady, Undergraduate Thesis (Houghton College, New York, 2017, unpublished).
  - [25] A. Raymond, J.W. Jewett Jr., *Physics for Scientists and Engineers with Modern Physics* (Cengage Learning, 2010).

---

[26] M. J. Buerger, PNAS **26**, 637 (1940).